

# Gaussian-SLAM: Photo-realistic Dense SLAM with Gaussian Splatting

Vladimir Yugay<sup>1</sup>, Yue Li<sup>1</sup>, Theo Gevers<sup>1</sup>, and Martin R. Oswald<sup>1</sup>

University of Amsterdam, Netherlands

[https://vladimiryugay.github.io/gaussian\\_slam](https://vladimiryugay.github.io/gaussian_slam)

**Abstract.** We present a dense simultaneous localization and mapping (SLAM) method that uses 3D Gaussians as a scene representation. Our approach enables interactive-time reconstruction and photo-realistic rendering from real-world single-camera RGBD videos. To this end, we propose a novel effective strategy for seeding new Gaussians for newly explored areas and their effective online optimization that is independent of the scene size and thus scalable to larger scenes. This is achieved by organizing the scene into sub-maps which are independently optimized and do not need to be kept in memory. We further accomplish frame-to-model camera tracking by minimizing photometric and geometric losses between the input and rendered frames. The Gaussian representation allows for high-quality photo-realistic real-time rendering of real-world scenes. Evaluation on synthetic and real-world datasets demonstrates competitive or superior performance in mapping, tracking, and rendering compared to existing neural dense SLAM methods.

## 1 Introduction

Simultaneous localization and mapping (SLAM) has been an active research topic for the past two decades [15, 22]. A major byproduct of that journey is the investigation of various scene representations to either push the tracking performance and mapping capabilities or to adapt it for more complex downstream tasks like path planning or semantic understanding. Specifically, earlier works focus on tracking using various scene representations like feature point clouds [14, 26, 42], surfels [56, 72], depth maps [45, 61], or implicit representations [13, 44, 46]. Later works focus more on the map quality and density. With the advent of powerful neural scene representations like neural radiance fields [40] that allow for high fidelity view-synthesis, a rapidly growing body of dense neural SLAM methods [18, 34, 53, 63, 65, 66, 85, 89] has been developed. Despite their impressive gains in scene representation quality, these methods are still limited to small synthetic scenes and their re-rendering results are far from photo-realistic.

Recently, a novel scene representation based on Gaussian splatting [25] has been shown to deliver on-par rendering performance with NeRFs while being an order of magnitude faster in rendering and optimization. Moreover, this scene representation is directly interpretable and can be directly manipulated which is desirable for many downstream tasks. With these advantages, the Gaussian

splatting representation lends itself to be applied in an online SLAM system with real-time demands and opens the door to photo-realistic dense SLAM.



**Fig. 1: Rendering Results of Gaussian-SLAM.** Embedded into a dense SLAM pipeline, the 3D Gaussian-based scene representation allows for fast, photo-realistic rendering of scene views. This leads to high-quality rendering, especially on real-world data like this TUM-RGBD [62] frame that contains many high-frequency details that other methods struggle to capture.

In this paper, we introduce Gaussian-SLAM, a dense RGBD SLAM system using 3D Gaussians to build a scene representation that allows for mapping, tracking, and photo-realistic re-rendering at interactive runtimes. An example of the high-fidelity rendering output of Gaussian-SLAM is depicted in Fig. 1. In summary, our **contributions** include:

- A dense RGBD SLAM approach that uses 3D Gaussians to construct a scene representation allowing SOTA rendering results on real-world scenes.
- An extension of Gaussian splatting that better encodes geometry and allows reconstruction beyond radiance fields in a single-camera setup.
- An online optimization method for Gaussian splats that processes the map as sub-maps and introduces efficient seeding and optimization strategies.
- A frame-to-model tracker with the Gaussian splatting scene representation via photometric and geometric error minimization.

All source code and data will be made publicly available.

## 2 Related Work

**Dense Visual SLAM and Online Mapping.** The seminal work of Curless and Levoy [11] set the stage for a variety of 3D reconstruction methods using truncated signed distance functions (TSDF). A line of works was built upon it improving speed [44] through efficient implementation and volume integration, scalability through voxel hashing [20,46,48] and octree data structure [57], as well as tracking with sparse image features [4] and loop closures [5,13,45,56]. Tackling the problem of unreliable depth maps, RoutedFusion [70] introduced a learning-based fusion network for updating the TSDF in volumetric grids. This concept was further evolved by NeuralFusion [71] and DI-Fusion [18], which adopt implicit learning for scene representation, enhancing their robustness against outliers. Recent research has successfully achieved dense online reconstruction using solely RGB cameras [3,8,27,43,55,58,64], bypassing the need for depth data.

Recently, test-time optimization methods have become popular due to their ability to adapt to unseen scenes on the fly. Continuous Neural Mapping [77], for instance, employs a continual mapping strategy from a series of depth maps to learn scene representation. Inspired by Neural Radiance Fields [40], there has been immense progress in dense surface reconstruction [47,67] and accurate pose estimation [2,29,52,69]. These efforts have led to the development of comprehensive dense SLAM systems [34,54,63,78,85,88,89], showing a trend in the pursuit of precise and reliable visual SLAM. A comprehensive survey on online RGBD reconstruction can be found in [90].

While the latest neural methods show impressive rendering capabilities on synthetic data, they struggle when applied to real-world data. Further, these methods are not yet practical for real-world applications due to computation requirements, slow speed, and the inability to effectively incorporate pose updates, as the neural representations rely on positional encoding. In contrast, our method shows impressive performance on real-world data, has competitive tracking and runtime, and uses a scene representation that naturally allows pose updates.

**Scene Representations for SLAM.** The majority of dense 3D scene representations for SLAM are grid-based, point-based, network-based, or hybrid. Among these, grid-based techniques are perhaps the most extensively researched. They further divide into methods using dense grids [3,9,11,28,44,64,70–73,86,87,89], hierarchical octrees [6,30,31,36,57,78] and voxel hashing [13,20,41,46,67] for efficient memory management. Grids offer the advantage of simple and quick neighborhood lookups and context integration. However, a key limitation is the need to predefine grid resolution, which is not easily adjustable during reconstruction. This can result in inefficient memory usage in empty areas while failing to capture finer details due to resolution constraints.

Point-based approaches address some of the grid-related challenges and have been effectively utilized in 3D reconstruction [5,7,10,21,24,56,72,83]. Unlike grid resolution, the density of points in these methods does not have to be predetermined and can naturally vary throughout the scene. Moreover, point

sets can be efficiently concentrated around surfaces, not spending memory on modeling empty space. The trade-off for this adaptability is the complexity of finding neighboring points, as point sets lack structured connectivity. In dense SLAM, this challenge can be mitigated by transforming the 3D neighborhood search into a 2D problem via projection onto keyframes [56, 72], or by organizing points within a grid structure for expedited searching [75].

Network-based methods for dense 3D reconstruction provide a continuous scene representation by implicitly modeling it with coordinate-based networks [1, 27, 38, 49, 63, 66, 67, 77, 79, 85]. This representation can capture high-quality maps and textures. However, they are generally unsuitable for online scene reconstruction due to their inability to update local scene regions and to scale for larger scenes. More recently, a hybrid representation combining the advantages of point-based and neural-based was proposed [53]. While addressing some of the issues of both representations it struggles with real-world scenes, and cannot seamlessly integrate trajectory updates in the scene representation.

Outside these three primary categories, some studies have explored alternative representations like surfels [16, 39] and neural planes [34, 51]. Parameterized surface elements are generally not great at modeling a flexible shape template while feature planes struggle with scene reconstructions containing multiple surfaces, due to their overly compressed representation. Recently, Kerbl *et al.* [25] proposed to represent a scene with 3D Gaussians. The Gaussian parameters are optimized via differential rendering with multi-view supervision. While being very efficient and achieving impressive rendering results, this representation is tailored for fully-observed multi-view environments and does not encode geometry well. Concurrent to our work, [74, 80, 81] focus on dynamic scene reconstruction, and [33] on tracking. However, they are all offline methods and do not suit single-camera dense SLAM setups.

Concurrently, several methods [17, 23, 37, 76] have used Gaussian Splatting [25] for SLAM. While most splatting-based methods use gradient-based map densification similar to [25], we follow a more controlled approach with exact thresholding by utilizing fast nearest-neighbor search and alpha masking. Further, unlike all other concurrent work, our mapping pipeline does not require holding all the 3D Gaussians in the GPU memory, allowing our method to scale and not slow down as more areas are covered. Moreover, while in concurrent works the 3D Gaussians are very densely seeded, our color gradient and masking-based seeding strategy allows for sparser seeding while preserving SOTA rendering quality. Finally, in contrast to [17, 37, 76], our tracking does not rely on explicitly computed camera pose derivatives and is implemented in PyTorch.

### 3 Method

The key idea of our approach is to construct a map using 3D Gaussians [25] as a main building block to make single-camera RGBD neural SLAM scalable, faster and achieve better rendering on real-world datasets. We introduce a novel efficient mapping process with bounded computational cost in a sequential single-

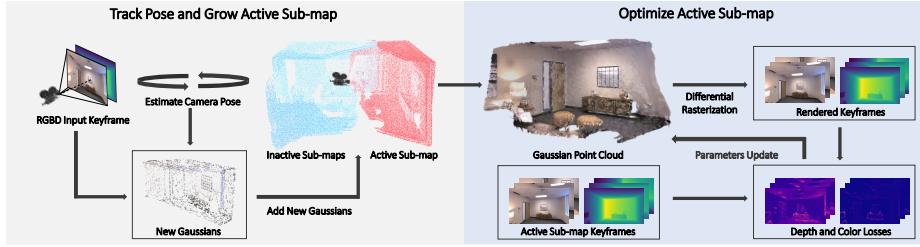


**Fig. 2: Gaussian-SLAM Architecture.** For every input keyframe the camera pose is estimated using depth and color losses against the *active* sub-map. Given an estimated camera pose, the RGBD frame is transformed into 3D and subsampled based on color gradient and the rendered alpha mask. Points from the subsampled point clouds located in low-density areas of the *active* sub-map are used to initialize new 3D Gaussians. These sparse 3D Gaussians are then added to the Gaussian point cloud of the *active* sub-map and are jointly optimized with the depth maps and color images from all contributing keyframes of this sub-map.

camera setup, a challenging scenario for traditional 3D Gaussian Splatting. To enable traditional Gaussian splats to render accurate geometry we extend them by adding a differential depth rendering, explicitly computing gradients for the Gaussian parameters updates. Finally, we develop a novel frame-to-model tracking approach relying on our 3D map representation. Fig. 2 provides an overview of our method. We now explain our pipeline, starting with an overview of classical Gaussian splatting [25], and continuing with map construction and optimization, geometry encoding, and tracking.

### 3.1 Gaussian Splatting

Gaussian splatting [25] is an effective method for representing 3D scenes with novel-view synthesis capability. This approach is notable for its speed, without compromising the rendering quality. In [25], 3D Gaussians are initialized from a sparse Structure-from-Motion point cloud of a scene. With images observing the scene from different angles, the Gaussian parameters are optimized using differentiable rendering. During training, 3D Gaussians are adaptively added or removed to better render the images based on a set of heuristics.

A single 3D Gaussian is parameterized by mean  $\mu \in \mathbb{R}^3$ , covariance  $\Sigma \in \mathbb{R}^{3 \times 3}$ , opacity  $o \in \mathbb{R}$ , and RGB color  $C \in \mathbb{R}^3$ . The mean of a projected (splatted) 3D Gaussian in the 2D image plane  $\mu^I$  is computed as follows:

$$\mu^I = \pi(P(T_{wc}\mu_{\text{homogeneous}})) , \quad (1)$$

where  $T_{wc} \in SE(3)$  is the world-to-camera transformation,  $P \in \mathbb{R}^{4 \times 4}$  is an OpenGL-style projection matrix,  $\pi : \mathbb{R}^4 \rightarrow \mathbb{R}^2$  is a projection to pixel coordinates. The 2D covariance  $\Sigma^I$  of a splatted Gaussian is computed as:

$$\Sigma^I = J R_{wc} \Sigma R_{wc}^T J^T , \quad (2)$$

where  $J \in \mathbb{R}^{2 \times 3}$  is an affine transformation from [91],  $R_{wc} \in SO(3)$  is the rotation component of world-to-camera transformation  $T_{wc}$ . We refer to [91] for further details about the projection matrices. Color  $C$  along one channel  $ch$  at a pixel  $i$  influenced by  $m$  ordered Gaussians is rendered as:

$$C_i^{ch} = \sum_{j \leq m} C_j^{ch} \cdot \alpha_j \cdot T_j, \text{ with } T_j = \prod_{k < j} (1 - \alpha_k), \quad (3)$$

with  $\alpha_j$  is computed as:

$$\alpha_j = o_j \cdot \exp(-\sigma_j) \quad \text{and} \quad \sigma_j = \frac{1}{2} \Delta_j^T \Sigma_j^{I-1} \Delta_j, \quad (4)$$

where  $\Delta_j \in \mathbb{R}^2$  is the offset between the pixel coordinates and the 2D mean of a splatted Gaussian. The parameters of the 3D Gaussians are iteratively optimized by minimizing the photometric loss between rendered and training images. During optimization,  $C$  is encoded with spherical harmonics  $SH \in \mathbb{R}^{15}$  to account for direction-based color variations. Covariance is decomposed as  $\Sigma = RSS^T R^T$ , where  $R \in \mathbb{R}^{3 \times 3}$  and  $S = \text{diag}(s) \in \mathbb{R}^{3 \times 3}$  are rotation and scale respectively to preserve covariance positive semi-definite property during gradient-based optimization.

### 3.2 3D Gaussian-based Map

To avoid catastrophic forgetting and overfitting and make the mapping computationally feasible in a single-camera stream scenario we process the input in chunks (sub-maps). Every sub-map covers several keyframes observing it and is represented with a separate 3D Gaussian point cloud. Formally, we define a sub-map Gaussian point cloud  $P^s$  as a collection of  $N$  3D Gaussians:

$$P^s = \{G(\mu_i^s, \Sigma_i^s, o_i^s, C_i^s) \mid i = 1, \dots, N\}. \quad (5)$$

**Sub-map Initialization.** A sub-map starts with the first frame and grows incrementally with newly incoming keyframes. As the explored area grows, a new sub-map is needed to cover the unseen regions and avoid storing all the Gaussians in GPU memory. Instead of using a fixed interval when creating a new sub-map [9, 13, 35], an initialization strategy that relies on the camera motion [5, 60] is used. Specifically, a new sub-map is created when the current frame’s estimated translation relative to the first frame of the active sub-map exceeds a predefined threshold,  $d_{\text{thre}}$ , or when the estimated Euler angle surpasses  $\theta_{\text{thre}}$ . At any time, only active sub-map is processed. This approach bounds the compute cost and ensures that optimization remains fast while exploring larger scenes.

**Sub-map Building.** Every new keyframe may add 3D Gaussians to the active sub-map to account for the newly observed parts of the scene. Following the pose estimation for the current keyframe, a dense point cloud is computed from keyframe RGBD measurements. At the beginning of each sub-map, we sample  $M_u$  uniformly and  $M_c$  points from the keyframe point cloud in high color gradient

regions to add new Gaussians. For the following keyframes of the sub-map, we sample  $M_k$  points uniformly from the regions with the rendered alpha values lower than a threshold  $\alpha_n$ . This allows for growing the map in areas sparsely covered by the 3D Gaussians. New Gaussians are added to the sub-map using sampled points that have no neighbors within a search radius  $\rho$  in the current sub-map. The new Gaussians are anisotropic and their scales are defined based on the nearest neighbor distance within the active sub-map. This densification strategy substantially differs from [25] where new Gaussians were added and pruned based on the gradient values during optimization and gives fine-grained control over the number of Gaussians.

**Sub-map Optimization.** All Gaussians in the active sub-map are jointly optimized every time new Gaussians are added to the sub-map for a fixed number of iterations minimizing the loss (12). We do not clone or prune the Gaussians as done in [25] during optimization to preserve geometry density obtained from the depth sensor, decrease computation time, and better control the number of Gaussians. We optimize the active sub-map to render the depth and color of all its keyframes. We directly optimize RGB color without using spherical harmonics to speed up optimization. In Gaussian splatting [25] the scene representation is optimized for many iterations over all the training views. However, this approach does not suit the SLAM setup where speed is crucial. Naively optimizing with an equal number of iterations for all keyframes results in underfitting or excessive time spent on optimization. We solve this by optimizing only the keyframes in the active sub-map and spending at least 40% of iterations on the new keyframe.

### 3.3 Geometry and Color Encoding

While Gaussian Splatting [25] is good at rendering images, the rendered depth maps are of limited accuracy since there is no direct depth supervision. We tackle this problem with an additional depth loss. To render the depth  $D_i$  at pixel  $i$  that is influenced by  $m$  ordered Gaussians we compute:

$$D_i = \sum_{j \leq m} \mu_j^z \cdot \alpha_j \cdot T_j \quad , \quad (6)$$

where  $\mu_j^z$  is a  $z$  component of the mean of a 3D Gaussian,  $\alpha_j$  and  $T_j$  are the same as in Eq. (3). To update the 3D Gaussian parameters based on the observed depth, we derive the gradients of the depth loss w.r.t. the 3D Gaussians' means, covariances, and opacity. Denoting the depth loss as  $L_{\text{depth}}$ , we follow the chain rule to compute the gradient for the mean update of the Gaussian  $j$ :

$$\frac{\partial L_{\text{depth}}}{\partial \mu_j} = \frac{\partial L_{\text{depth}}}{\partial D_i} \frac{\partial D_i}{\partial \alpha_j} \frac{\partial \alpha_j}{\partial \mu_j} \quad , \quad (7)$$

where  $\frac{\partial L_{\text{depth}}}{\partial D_i}$  is computed with PyTorch autograd using Eq. (9) and  $\frac{\partial \alpha_j}{\partial \mu_j}$  is derived as in [25]. We derive  $\frac{\partial D_i}{\partial \alpha_j}$  as:

$$\frac{\partial D_i}{\partial \alpha_j} = \mu_j^z \cdot T_j - \frac{\sum_{u > j} \mu_u^z \alpha_u T_u}{1 - \alpha_j} \quad . \quad (8)$$

The gradients for covariance and opacity are computed similarly. Apart from  $\frac{\partial L_{\text{depth}}}{\partial D_i}$ , all gradients are explicitly computed in CUDA to preserve the optimization speed of the unified rendering pipeline. For depth supervision, we use the loss:

$$L_{\text{depth}} = |\hat{D} - D|_1 , \quad (9)$$

with  $D$  and  $\hat{D}$  being the ground-truth and reconstructed depth maps, respectively. For the color supervision we use a weighted combination of  $L_1$  and SSIM [68] losses:

$$L_{\text{color}} = (1 - \lambda) \cdot |\hat{I} - I|_1 + \lambda(1 - \text{SSIM}(\hat{I}, I)) , \quad (10)$$

where  $I$  is the original image,  $\hat{I}$  is the rendered image, and  $\lambda = 0.2$ .

When seeded sparsely as in our case, a few 3D Gaussians sometimes elongate too much in scale. To overcome this, we add an isotropic regularization term  $L_{\text{reg}}$  when optimizing a sub-map  $K$ :

$$L_{\text{reg}} = \frac{\sum_{k \in K} |s_k - \bar{s}_k|}{|K|} , \quad (11)$$

where  $s_k \in \mathbb{R}^3$  is the scale of a 3D Gaussian,  $\bar{s}_k$  is the mean sub-map scale, and  $|K|$  is the number of Gaussians in the sub-map. Finally, we optimize color, depth, and regularization terms together:

$$L = \lambda_{\text{color}} \cdot L_{\text{color}} + \lambda_{\text{depth}} \cdot L_{\text{depth}} + \lambda_{\text{reg}} \cdot L_{\text{reg}} , \quad (12)$$

where  $\lambda_{\text{color}}, \lambda_{\text{depth}}, \lambda_{\text{reg}} \in \mathbb{R}_{\geq 0}$  are weights for the corresponding losses.

### 3.4 Tracking

We perform frame-to-model tracking based on the mapped scene. We initialize the current camera pose  $T_i$  with a constant speed assumption:

$$T_i = T_{i-1} + (T_{i-1} - T_{i-2}) , \quad (13)$$

where pose  $T_i = \{\mathbf{q}_i, \mathbf{t}_i\}$  encodes a quaternion and translation vector. To estimate the camera pose we minimize the tracking loss  $L_{\text{tracking}}$  with respect to relative camera pose  $T_{i-1,i}$  between frames  $i-1$  and  $i$  as follows:

$$\arg \min_{T_{i-1,i}} L_{\text{tracking}} \left( \hat{I}(T_{i-1,i}), \hat{D}(T_{i-1,i}), I_i, D_i, \alpha \right) , \quad (14)$$

where  $\hat{I}(T_{i-1,i})$  and  $\hat{D}(T_{i-1,i})$  are the rendered color and depth from the sub-map transformed with the relative transformation  $T_{i-1,i}$ ,  $C_i$  and  $D_i$  are the input color and depth map at frame  $i$ .

We introduce soft alpha and error masking to not contaminate the tracking loss with the pixels from previously unobserved or poorly reconstructed areas. Soft alpha mask  $M_{\text{alpha}}$  is a polynomial of the alpha map rendered directly from



the active sub-map. Error boolean mask  $M_{\text{inlier}}$  discards all the pixels where the color and depth errors are larger than a frame-relative error threshold:

$$L_{\text{tracking}} = \sum M_{\text{inlier}} \cdot M_{\text{alpha}} \cdot (\lambda_c |\hat{I} - I|_1 + (1 - \lambda_c) |\hat{D} - D|_1). \quad (15)$$

The weighting ensures the optimization is guided by well-reconstructed regions where the accumulated alpha values are close to 1 and rendering quality is high. During optimization, all the 3D Gaussian parameters are frozen.

## 4 Experiments

We first describe our experimental setup and then evaluate our method against state-of-the-art dense neural RGBD SLAM methods on synthetic [59] and real-world datasets [12, 62, 82]. In addition, we compare our method with concurrent work with released source code. The reported results are the average of 3 runs using different seeds. The tables highlight best results as [first](#), [second](#), [third](#).

**Implementation Details.** We set  $M_u = 600000$  for Replica [59], 100000 for TUM-RGBD [62] and ScanNet [12], and 400000 for ScanNet++ [82].  $M_c$  is set to 50000 for all datasets. For the first keyframe in a sub-map, the number of mapping iterations is set to 1,000 for Replica, 100 for TUM-RGBD and ScanNet, and 500 for ScanNet++. For the subsequent keyframes in a sub-map, the iteration count is set to 100 across all datasets. Every 5th frame is considered as a keyframe for all the datasets. When selecting point candidates from subsequent keyframes, we use alpha threshold  $\alpha_n = 0.6$ . We use FAISS [19] GPU implementation to find nearest neighbors when choosing point candidates to add as new Gaussians and set the search radius  $\rho = 0.01 m$  for all the datasets. For new sub-map initialization, we set  $d_{\text{thre}} = 0.5 m$  and  $\theta_{\text{thre}} = 50^\circ$ . For sub-map optimization, the best results were obtained with  $\lambda_{\text{color}}$ ,  $\lambda_{\text{reg}}$  and  $\lambda_{\text{depth}}$  to 1. We spend at least 40% mapping iterations on the newly added keyframe during sub-map optimization. To mesh the scene, we render depth and color every fifth frame over the estimated trajectory and use TSDF Fusion [11] with voxel size 1 cm similar to [53]. Further details are provided in the supplement.

**Datasets.** The Replica dataset [59] comprises high-quality 3D reconstructions of a variety of indoor scenes. We utilize the publicly available dataset collected by Sucar *et al.* [63], which provides trajectories from an RGBD sensor. Further, we demonstrate that our framework achieves SOTA results on real-world data by using the TUM-RGBD [62], ScanNet [12] and ScanNet++ [82] datasets. The poses for TUM-RGBD were captured using an external motion capture system while ScanNet uses poses estimated by BundleFusion [13], and ScanNet++ obtains poses by registering the images with a laser scan. Since ScanNet++ is not specifically designed for benchmarking neural SLAM, it has larger camera movements. Therefore, we choose 5 scenes where the first 250 frames are smooth in trajectory and use them for benchmarking.

**Evaluation Metrics.** To assess tracking accuracy, we use ATE RMSE [62], and for rendering we compute PSNR, SSIM [68] and LPIPS [84]. All rendering

metrics are evaluated by rendering full-resolution images along the estimated trajectory with mapping intervals similar to [53]. We also follow [53] to measure reconstruction performance on meshes produced by marching cubes [32]. The reconstructions are also evaluated using the F1-score - the harmonic mean of the Precision (P) and Recall (R). We use a distance threshold of 1 cm for all evaluations. We further provide the depth L1 metric for unseen views as in [89].

**Baseline Methods.** We primarily compare our method to existing state-of-the-art dense neural RGBD SLAM methods such as NICE-SLAM [89], Vox-Fusion [78], ESLAM [34], and Point-SLAM [53]. In addition, we compare against the concurrent work using the released code [23].

**Rendering Performance.** Tab. 1 compares rendering performance and shows improvements over all the existing dense neural RGBD SLAM methods on synthetic data. Tab. 2 and Tab. 3 show our state-of-the-art rendering performance on real-world datasets. Fig. 3 shows exemplary full-resolution renderings where Gaussian-SLAM yields more accurate details. Qualitative results on novel views are provided as a video in the supplementary.

**Table 1: Rendering Performance on Replica [59].** We outperform all existing dense neural RGBD methods on the commonly reported rendering metrics. Concurrent work is marked with an asterisk\*.

Method	Metric	Rm0	Rm1	Rm2	Off0	Off1	Off2	Off3	Off4	Avg.
NICE-SLAM [89]	PSNR $\uparrow$	22.12	22.47	24.52	29.07	30.34	19.66	22.23	24.94	24.42
	SSIM $\uparrow$	0.689	0.757	0.814	0.874	0.886	0.797	0.801	0.856	0.809
	LPIPS $\downarrow$	0.330	0.271	0.208	0.229	0.181	0.235	0.209	0.198	0.233
Vox-Fusion [78]	PSNR $\uparrow$	22.39	22.36	23.92	27.79	29.83	20.33	23.47	25.21	24.41
	SSIM $\uparrow$	0.683	0.751	0.798	0.857	0.876	0.794	0.803	0.847	0.801
	LPIPS $\downarrow$	0.303	0.269	0.234	0.241	0.184	0.243	0.213	0.199	0.236
ESLAM [34]	PSNR $\uparrow$	25.25	27.39	28.09	30.33	27.04	27.99	29.27	29.15	28.06
	SSIM $\uparrow$	0.874	0.89	0.935	0.934	0.910	0.942	0.953	0.948	0.923
	LPIPS $\downarrow$	0.315	0.296	0.245	0.213	0.254	0.238	0.186	0.210	0.245
Point-SLAM [53]	PSNR $\uparrow$	32.40	34.08	35.50	38.26	39.16	33.99	33.48	33.49	35.17
	SSIM $\uparrow$	0.974	0.977	0.982	0.983	0.986	0.960	0.960	0.979	0.975
	LPIPS $\downarrow$	0.113	0.116	0.111	0.100	0.118	0.156	0.132	0.142	0.124
SplaTAM* [23]	PSNR $\uparrow$	32.86	33.89	35.25	38.26	39.17	31.97	29.70	31.81	34.11
	SSIM $\uparrow$	0.98	0.97	0.98	0.98	0.98	0.97	0.95	0.95	0.97
	LPIPS $\downarrow$	0.07	0.10	0.08	0.09	0.09	0.10	0.12	0.15	0.10
Gaussian-SLAM (ours)	PSNR $\uparrow$	<b>38.88</b>	<b>41.80</b>	<b>42.44</b>	<b>46.40</b>	<b>45.29</b>	<b>40.10</b>	<b>39.06</b>	<b>42.65</b>	<b>42.08</b>
	SSIM $\uparrow$	<b>0.993</b>	<b>0.996</b>	<b>0.996</b>	<b>0.998</b>	<b>0.997</b>	<b>0.997</b>	<b>0.997</b>	<b>0.997</b>	<b>0.996</b>
	LPIPS $\downarrow$	<b>0.017</b>	<b>0.018</b>	<b>0.019</b>	<b>0.015</b>	<b>0.016</b>	<b>0.020</b>	<b>0.020</b>	<b>0.020</b>	<b>0.018</b>

**Tracking Performance.** In Tab. 4, Fig. 4, Tab. 5 and Tab. 6 we report the tracking accuracy. Our method outperforms the nearest competitor by 14% on [59]. On TUM-RGBD dataset [62], Gaussian-SLAM also performs better than all baseline methods. On ScanNet dataset, our method exhibits a drift due to low-quality depth maps and a large amount of motion blur. On ScanNet++, our Gaussian splatting-based method performs significantly better than NeRF-

**Table 2: Rendering Performance on TUM-RGBD [62].** We outperform existing dense neural RGBD methods on the commonly reported rendering metrics. For qualitative results, see Fig. 3. Concurrent work is marked with an asterisk\*.

Method	Metric	fr1/desk	fr2/xyz	fr3/office	Avg.
NICE-SLAM [89]	PSNR↑	13.83	17.87	12.890	14.86
	SSIM↑	0.569	0.718	0.554	0.614
	LPIPS↓	0.482	0.344	0.498	0.441
Vox-Fusion [78]	PSNR↑	15.79	16.32	17.27	16.46
	SSIM↑	0.647	0.706	0.677	0.677
	LPIPS↓	0.523	0.433	0.456	0.471
ESLAM [34]	PSNR↑	11.29	17.46	17.02	15.26
	SSIM↑	0.666	0.310	0.457	0.478
	LPIPS↓	0.358	0.698	0.652	0.569
Point-SLAM [53]	PSNR↑	13.87	17.56	18.43	16.62
	SSIM↑	0.627	0.708	0.754	0.696
	LPIPS↓	0.544	0.585	0.448	0.526
SplaTAM* [23]	PSNR↑	22.00	24.50	21.90	22.80
	SSIM↑	0.857	0.947	0.876	0.893
	LPIPS↓	0.232	0.100	0.202	0.178
Gaussian-SLAM (ours)	PSNR↑	24.01	25.02	26.13	25.05
	SSIM↑	0.924	0.924	0.939	0.929
	LPIPS↓	0.178	0.186	0.141	0.168

**Table 3: Rendering Performance on ScanNet [12].** We outperform existing dense neural RGBD methods on the commonly reported rendering metrics by a significant margin. For qualitative results, see Fig. 3. Concurrent work is marked with an asterisk\*.

Method	Metric	0000	0059	0106	0169	0181	0207	Avg.
NICE-SLAM [89]	PSNR↑	18.71	16.55	17.29	18.75	15.56	18.38	17.54
	SSIM↑	0.641	0.605	0.646	0.629	0.562	0.646	0.621
	LPIPS↓	0.561	0.534	0.510	0.534	0.602	0.552	0.548
Vox-Fusion [78]	PSNR↑	19.06	16.38	18.46	18.69	16.75	19.66	18.17
	SSIM↑	0.662	0.615	0.753	0.650	0.666	0.696	0.673
	LPIPS↓	0.515	0.528	0.439	0.513	0.532	0.500	0.504
ESLAM [34]	PSNR↑	15.70	14.48	15.44	14.56	14.22	17.32	15.29
	SSIM↑	0.687	0.632	0.628	0.656	0.696	0.653	0.658
	LPIPS↓	0.449	0.450	0.529	0.486	0.482	0.534	0.488
Point-SLAM [53]	PSNR↑	21.30	19.48	16.80	18.53	22.27	20.56	19.82
	SSIM↑	0.806	0.765	0.676	0.686	0.823	0.750	0.751
	LPIPS↓	0.485	0.499	0.544	0.542	0.471	0.544	0.514
SplaTAM* [23]	PSNR↑	19.33	19.27	17.73	21.97	16.76	19.8	19.14
	SSIM↑	0.660	0.792	0.690	0.776	0.683	0.696	0.716
	LPIPS↓	0.438	0.289	0.376	0.281	0.420	0.341	0.358
Gaussian-SLAM(ours)	PSNR↑	28.539	26.208	26.258	28.604	27.789	28.627	27.67
	SSIM↑	0.926	0.9336	0.9259	0.917	0.9223	0.9135	0.923
	LPIPS↓	0.271	0.211	0.217	0.226	0.277	0.288	0.248

based methods. In addition, Gaussian-SLAM demonstrates greater robustness compared to alternative approaches.

**Reconstruction Performance.** In Tab. 7 we compare our method to NICE-SLAM [89], Vox-Fusion [78], ESLAM [34], Point-SLAM [53], and concurrent SplaTAM [23] in terms of the geometric reconstruction accuracy on the Replica dataset [59]. Our method performs on par with other existing dense SLAM methods.

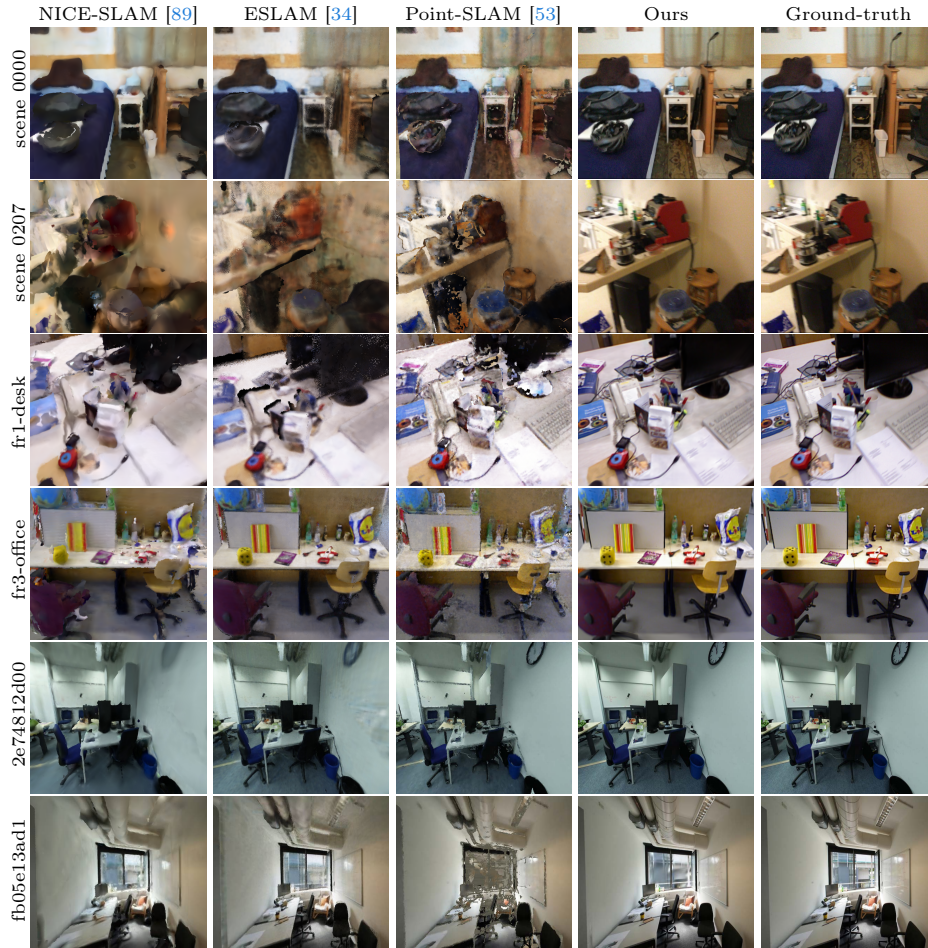


**Fig. 3: Rendering performance on ScanNet [12], TUM-RGBD [61] and ScanNet++ [82].** Thanks to 3D Gaussian splatting, Gaussian-SLAM can encode more high-frequency details and substantially increase the quality of the renderings (please zoom in for a better view of the details). This is also supported by the quantitative results in Tab. 2 and Tab. 3.

**Table 4: Tracking Performance on Replica [59] (ATE RMSE ↓ [cm]).** We outperform all other methods in on Replica. Concurrent work is marked with an asterisk\*.

Method	Rm0	Rm1	Rm2	Off0	Off1	Off2	Off3	Off4	Avg.
NICE-SLAM [89]	1.69	2.04	1.55	0.99	0.90	1.39	3.97	3.08	1.95
Vox-Fusion [78]	<b>0.27</b>	1.33	0.47	0.70	1.11	0.46	<b>0.26</b>	0.58	0.65
ESLAM [34]	0.71	0.70	0.52	0.57	0.55	0.58	0.72	0.63	0.63
Point-SLAM [53]	0.61	0.41	0.37	0.38	0.48	0.54	0.72	0.63	0.52
SplaTAM* [23]	0.31	0.40	0.29	0.47	0.27	<b>0.29</b>	0.32	0.55	0.36
Gaussian SLAM (ours)	0.29	<b>0.29</b>	<b>0.22</b>	<b>0.37</b>	<b>0.23</b>	0.41	0.30	<b>0.35</b>	<b>0.31</b>

Method	desk xyz office Avg.				Alpha Inlier ATE RMSE PSNR			
	mask	mask	mask	Avg.	mask	mask	[cm]↓	[dB]↑
NICE-SLAM [89]	4.3	31.7	3.9	13.3				
Vox-Fusion [78]	3.5	1.5	26.0	10.3	✗	✗	12.77	22.96
Point-SLAM [53]	4.3	1.3	<b>3.5</b>	3.0	✓	✗	2.68	24.01
SplaTAM* [23]	3.4	<b>1.2</b>	5.2	3.3	✗	✓	8.96	23.66
Gaussian SLAM	<b>2.6</b>	1.3	4.6	<b>2.9</b>	✓	✓	<b>2.50</b>	<b>24.32</b>

**Fig. 4: Tracking Performance on TUM-RGBD [62]** (ATE RMSE↓ [cm]). Our method outperforms all other methods on TUM\_RGBD. Concurrent work is marked with an asterisk\*.

**Fig. 5: Tracking Mask Ablation on desk.** Applying alpha and inlier masks to the tracking loss improves tracking leading to better rendering.

**Table 5: Tracking Performance on ScanNet [12]** (ATE RMSE↓ [cm]). Tracking on ScanNet is especially challenging due to low-quality depth maps and motion blur.

Method	0000	0059	0106	0169	0181	0207	Avg.
NICE-SLAM [89]	12.00	14.00	<b>7.90</b>	<b>10.90</b>	13.40	<b>6.20</b>	<b>10.70</b>
Vox-Fusion [78]	68.84	24.18	8.41	27.28	23.30	9.41	26.90
Point-SLAM [53]	<b>10.24</b>	<b>7.81</b>	8.65	22.16	14.77	9.54	12.19
SplaTAM* [23]	12.83	10.10	17.72	12.08	<b>11.10</b>	7.46	11.88
Gaussian SLAM	24.75	8.63	11.27	14.59	18.70	14.36	15.38

**Table 6: Tracking Performance on ScanNet++ [82]** (ATE RMSE ↓ [cm]). Our tracking proves to be robust and competitive in various real-world scenes.

Method	b20a261fdf	8b5caf3398	fb05e13ad1	2e74812d00	281bc17764	Avg.
Point-SLAM [53]	246.16	632.99	830.79	271.42	574.86	511.24
ESLAM [34]	25.15	2.15	27.02	20.89	35.47	22.14
SplaTAM* [23]	1.50	<b>0.57</b>	<b>0.31</b>	443.10	1.58	89.41
Gaussian SLAM (ours)	<b>1.37</b>	5.97	2.70	<b>2.35</b>	<b>1.02</b>	<b>2.68</b>

**Table 7: Reconstruction Performance on Replica [59].** Our method is comparable to the SOTA baseline Point-SLAM [53] which requires ground truth depth maps for inference while superior to other dense SLAM methods. Concurrent work is marked with an asterisk\*.

Method	Metric	Rm0	Rm1	Rm2	Off0	Off1	Off2	Off3	Off4	Avg.
NICE-SLAM [89]	Depth L1 [cm]↓	1.81	1.44	2.04	1.39	1.76	8.33	4.99	2.01	2.97
	F1 [%]↑	45.0	44.8	43.6	50.0	51.9	39.2	39.9	36.5	43.9
Vox-Fusion [78]	Depth L1 [cm]↓	1.09	1.90	2.21	2.32	3.40	4.19	2.96	1.61	2.46
	F1 [%]↑	69.9	34.4	59.7	46.5	40.8	51.0	64.6	50.7	52.2
ESLAM [34]	Depth L1 [cm] ↓	0.97	1.07	1.28	0.86	1.26	1.71	<b>1.43</b>	1.06	1.18
	F1 [%] ↑	81.0	82.2	83.9	78.4	75.5	77.1	75.5	79.1	79.1
Point-SLAM [53]	Depth L1 [cm]↓	<b>0.53</b>	<b>0.22</b>	<b>0.46</b>	<b>0.30</b>	0.57	<b>0.49</b>	<b>0.51</b>	0.46	<b>0.44</b>
	F1 [%]↑	86.9	<b>92.3</b>	<b>90.8</b>	<b>93.8</b>	<b>91.6</b>	<b>89.0</b>	<b>88.2</b>	85.6	<b>89.8</b>
SplaTAM* [23]	Depth L1 [cm]↓	<b>0.43</b>	0.38	0.54	0.44	0.66	1.05	1.60	0.68	0.72
	F1 [%]↑	<b>89.3</b>	88.2	88.0	91.7	90.0	85.1	77.1	80.1	86.1
Gaussian SLAM (ours)	Depth L1 [cm]↓	0.61	0.25	0.54	0.50	<b>0.52</b>	0.98	1.63	<b>0.42</b>	0.68
	F1 [%]↑	88.8	91.4	90.5	91.7	90.1	87.3	84.2	<b>87.4</b>	88.9

**Runtime Comparison.** In Tab. 8 we compare runtime usage on the Replica office0 scene. We report both per-iteration and per-frame runtime. The per-frame runtime is calculated as the optimization time spent on all mapped frames divided by sequence length, while the per-iteration runtime is the average mapping iteration time.

**Table 8: Average Mapping, Tracking, and Rendering Speed on Replica office0.** Per-frame runtime is calculated as the total optimization time divided by sequence length. All metrics are profiled using an NVIDIA RTX A6000 GPU.

Method	Mapping /Iteration(ms)	Mapping /Frame(s)	Tracking /Iteration(ms)	Tracking /Frame(s)	Rendering (FPS)
NICE-SLAM [89]	89	1.15	27	1.06	2.64
Vox-Fusion [78]	98	1.47	64	1.92	1.63
ESLAM [34]	30	<b>0.62</b>	18	<b>0.15</b>	0.65
Point-SLAM [53]	57	3.52	27	1.11	2.96
SplaTAM* [23]	81	4.89	67	2.70	<b>2175</b>
Gaussian-SLAM (ours)	<b>24</b>	0.93	<b>14</b>	0.83	<b>2175</b>

**Ablation Study.** In Fig. 5 we ablate the effectiveness of soft alpha mask  $M_{\text{alpha}}$  and inlier mask  $M_{\text{inlier}}$  for the tracking performance on TUM-RGBD fr1/desk scene. It demonstrates the effectiveness of both masks with the soft alpha mask having more performance impact.

**Limitations and Future Work.** Although we have effectively used 3D Gaussians for online dense SLAM, tracking a camera trajectory on data with lots of motion blur and low-quality depth maps remains challenging. We also believe that some of our empirical hyperparameters like keyframe selection strategy can be made test time adaptive or learned. Finally, trajectory drift is inevitable in frame-to-model tracking without additional techniques like loop-closure or bundle adjustment which might be an interesting future work.

## 5 Conclusion

We introduced Gaussian-SLAM, a dense SLAM system based on 3D Gaussian Splatting as the scene representation that enables unprecedented re-rendering capabilities. We proposed effective strategies for efficient seeding and online optimization of 3D Gaussians, their organization in sub-maps for better scalability, and a frame-to-model tracking algorithm. Compared to previous SOTA neural SLAM systems like Point-SLAM [53] we achieve faster tracking and mapping while obtaining better rendering results on synthetic and real-world datasets. We demonstrated that Gaussian-SLAM yields top results in rendering, camera pose estimation, and scene reconstruction on a variety of datasets.

## A Abstract

This supplementary material accompanies the main paper by providing further information for better reproducibility as well as additional evaluations and qualitative results.

## B Further Implementation Details

The inlier mask  $M_{\text{inlier}}$  in tracking loss filters out pixels that have depth errors 50 times larger than the median depth error of the current re-rendered depth map. Pixels without valid depth input are also excluded as the inconsistent re-rendering in those areas can misguide the pose optimization. For soft alpha mask, we adopt  $M_{\text{alpha}} = \alpha^3$  for per-pixel loss weighting. The opacity values for added Gaussians are initialized as 0.5 and their initial scales are set to the nearest neighbor distances in the active sub-map. At the middle and the end of mapping iterations on new keyframes, we prune Gaussians having opacity values lower than a threshold  $o_{\text{thre}}$ . We set  $o_{\text{thre}} = 0.1$  for Replica [59] and 0.5 for all other datasets. Additionally, we use multi-scale RGBD odometry [50] to help initialize the pose for tracking optimization on Replica dataset, for all other datasets, we use pose initialization based on constant speed assumption. On Scannet++ dataset [82], if at the initialized pose, the re-rendering loss is 50 times larger than the running average of the re-rendering loss after tracking optimization, we use the odometry to re-initialize the pose for the current frame.

Upon completing the pipeline for the input sequence, we merge the saved sub-maps into a global map. Specifically, we select Gaussians from each sub-map in sequence as candidates and add them using the same nearest neighbor checking rule as in the sub-map building. Finally, as a post-processing step, we perform color refinement on the global map for 10000 iterations.

## C Additional Experiments

**Isotropic Regularization Ablation.** In Tab. 9 and Tab. 10 we ablate the isotropic regularization term  $L_{\text{reg}}$  in the mapping loss. On Replica dataset [59], where the RGBD inputs are synthetic and noise-free, the  $L_{\text{reg}}$  terms improves both tracking and rendering performance marginally. While on real-world TUM-RGBD dataset [61],  $L_{\text{reg}}$  proves critical for accurate camera tracking. Fig. 6 further examines the underlying Gaussians on `fr1/desk` scene at a held-out view. Without isotropic regularization, the elongated Gaussians are evident. While they slightly enhance rendering by overfitting to training views, they are detrimental to pose optimization, which relies on re-rendering at novel views.

**Qualitative Reconstruction Results.** Fig. 7 shows reconstructed mesh on Replica dataset with a normal map shader to highlight the difference. Fig. 8 compares colored mesh on ScanNet [12] and TUM-RGBD scenes. Gaussian-SLAM can recover more geometric and color details in real-world reconstructions.

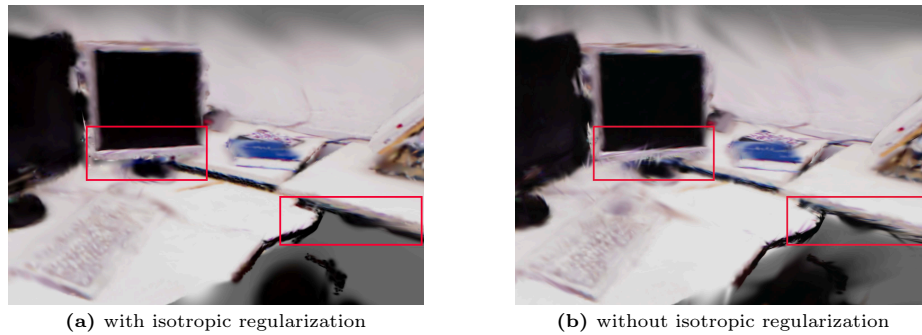
**Table 9: Isotropic Regularization Ablation on Replica dataset [59].** The regularization term  $L_{\text{reg}}$  improves both tracking and rendering performance.

Metric	$L_{\text{reg}}$	Rm0	Rm1	Rm2	Off0	Off1	Off2	Off3	Off4	Avg.
ATE ↓	✗	<b>0.25</b>	0.36	0.27	0.52	<b>0.23</b>	<b>0.37</b>	<b>0.30</b>	0.41	0.34
	✓	0.29	<b>0.29</b>	<b>0.22</b>	<b>0.37</b>	<b>0.23</b>	0.41	<b>0.30</b>	<b>0.35</b>	<b>0.31</b>
PSNR ↑	✗	38.83	41.71	42.18	46.12	44.72	39.72	38.94	42.58	41.85
	✓	<b>38.88</b>	<b>41.80</b>	<b>42.44</b>	<b>46.40</b>	<b>45.29</b>	<b>40.10</b>	<b>39.06</b>	<b>42.65</b>	<b>42.08</b>

**Table 10: Isotropic Regularization Ablation on TUM-RGBD dataset [61].** The regularization term  $L_{\text{reg}}$  is critical for tracking accuracy and improves the rendering performance.

Metric	$L_{\text{reg}}$	fr1/desk	fr2/xyz	fr3/office	Average
ATE ↓	✗	2.7	22.4	4.7	9.9
	✓	<b>2.6</b>	<b>1.3</b>	<b>4.6</b>	<b>2.9</b>
PSNR ↑	✗	<b>24.50</b>	23.03	<b>26.60</b>	24.71
	✓	24.01	<b>25.02</b>	26.13	<b>25.05</b>

**Novel View Synthesis.** In Tab. 11 we report the novel view synthesis results on the selected Scannet++ [82] scenes. The evaluated novel views in this dataset are not sampled from the input stream, but held-out views, which can better assess the extrapolation capability of the method. Gaussian-SLAM demonstrates clear advantage and outperforms concurrent work [23] by an average of 3.6 dB in PSNR. Qualitative rendering results are provided in Fig. 9.

**Fig. 6: Gaussians splatted at a held-out view in the mapped fr1/desk scene.** Notice the highlighted areas in red rectangles, where elongated Gaussians are clearly noticeable if isotropic regularization is not applied.



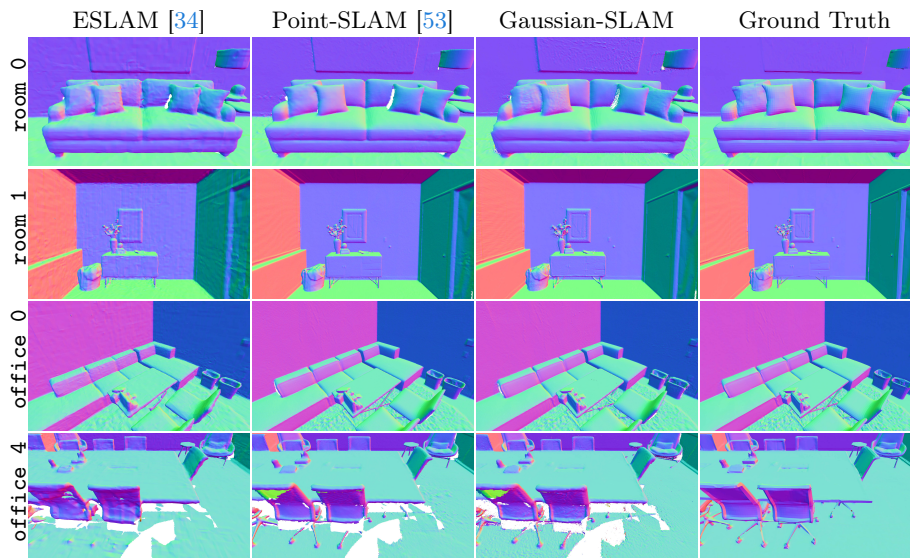


**Fig. 7: Qualitative Reconstruction Comparison on the Replica dataset [59].** Results are rendered with a normal map shader. Gaussian-SLAM achieves comparable reconstruction performance with the state-of-the-art dense neural SLAM methods.

**Table 11: Novel View Synthesis Performance on ScanNet++ dataset [82]** (PSNR  $\uparrow$  [dB]). Gaussian-SLAM demonstrates a clear advantage, outperforming concurrent work [23] by an average of 3.6 dB in PSNR for held-out views. Our calculation includes all pixels, regardless of whether they have valid depth input.

Method	b20a261fdf	8b5caf3398	fb05e13ad1	2e74812d00	281bc17764	Average
ESLAM [34]	13.63	11.86	11.83	10.59	10.64	11.71
SplaTAM [23]	23.95	22.66	13.95	8.47	20.06	17.82
Gaussian-SLAM	<b>25.92</b>	<b>24.49</b>	<b>16.36</b>	<b>18.56</b>	<b>22.04</b>	<b>21.47</b>

## References

1. Azinović, D., Martin-Brualla, R., Goldman, D.B., Nießner, M., Thies, J.: Neural rgb-d surface reconstruction. In: IEEE/CVF Conference on Computer Vision and Pattern Recognition. pp. 6290–6301 (2022) 4
2. Bian, W., Wang, Z., Li, K., Bian, J.W., Prisacariu, V.A.: Nope-nerf: Optimising neural radiance field with no pose prior. arXiv preprint arXiv:2212.07388 (2022) 3
3. Božič, A., Palafox, P., Thies, J., Dai, A., Nießner, M.: Transformerfusion: Monocular rgb scene reconstruction using transformers. arXiv preprint arXiv:2107.02191 (2021) 3
4. Bylow, E., Olsson, C., Kahl, F.: Robust online 3d reconstruction combining a depth sensor and sparse feature points. In: 2016 23rd International Conference on Pattern Recognition (ICPR). pp. 3709–3714 (2016) 3

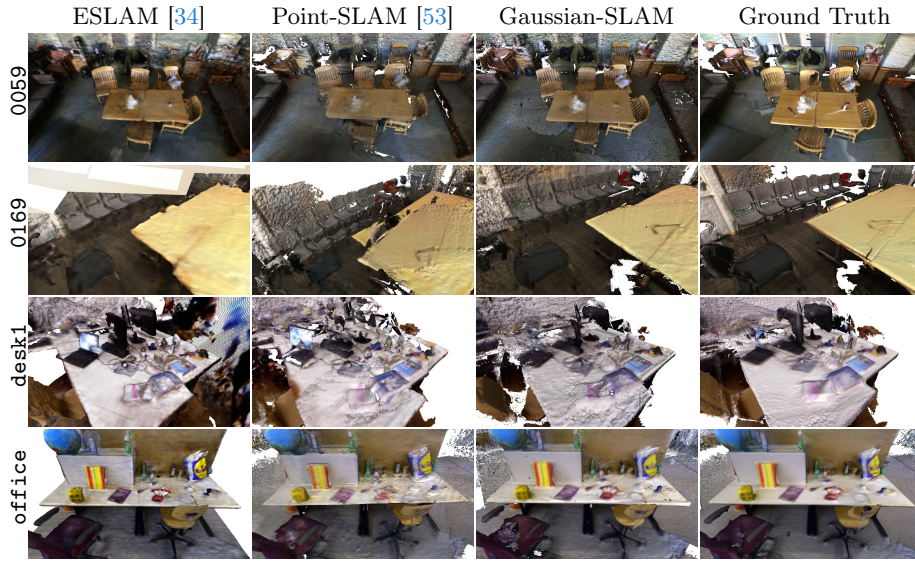


**Fig. 8: Qualitative Mesh-based Comparison on ScanNet [12] and TUM-RGBD [61] datasets.** For TUM-RGBD, the ground truth is obtained by TSDF fusion. NICE-SLAM [89] shows over-smoothed surfaces. Point-SLAM [53] has duplicated geometry. ESLAM [34] improves the reconstruction, while Gaussian-SLAM is moderately better in recovering geometric details, see the chairs in `scene_0059` for example.

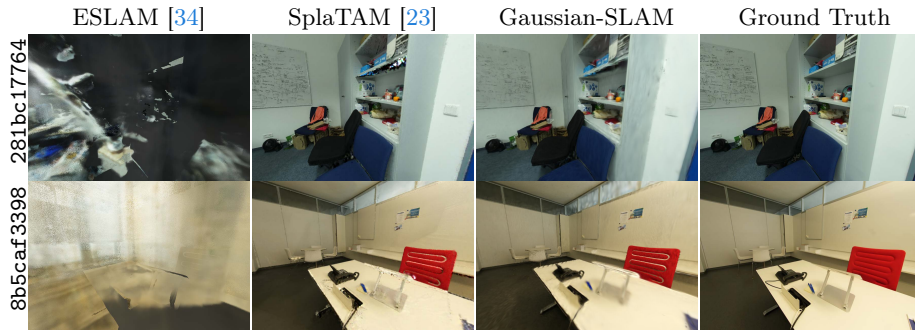


**Fig. 9: Qualitative Novel View Synthesis Comparison on the ScanNet++ dataset [82].** Gaussian-SLAM renders least artifacts at held-out views.

- Cao, Y.P., Kobbelt, L., Hu, S.M.: Real-time high-accuracy three-dimensional reconstruction with consumer rgb-d cameras. *ACM Transactions on Graphics (TOG)* **37**(5), 1–16 (2018) [3](#), [6](#)

6. Chen, J., Bautembach, D., Izadi, S.: Scalable real-time volumetric surface reconstruction. *ACM Transactions on Graphics (ToG)* **32**(4), 1–16 (2013) [3](#)
7. Cho, H.M., Jo, H., Kim, E.: Sp-slam: Surfel-point simultaneous localization and mapping. *IEEE/ASME Transactions on Mechatronics* **27**(5), 2568–2579 (2021) [3](#)
8. Choe, J., Im, S., Rameau, F., Kang, M., Kweon, I.S.: Volumefusion: Deep depth fusion for 3d scene reconstruction. In: *IEEE/CVF International Conference on Computer Vision (ICCV)*. pp. 16086–16095 (October 2021) [3](#)
9. Choi, S., Zhou, Q.Y., Koltun, V.: Robust reconstruction of indoor scenes. In: *Proceedings of the IEEE conference on computer vision and pattern recognition*. pp. 5556–5565 (2015) [3](#), [6](#)
10. Chung, C.M., Tseng, Y.C., Hsu, Y.C., Shi, X.Q., Hua, Y.H., Yeh, J.F., Chen, W.C., Chen, Y.T., Hsu, W.H.: Orbeez-slam: A real-time monocular visual slam with orb features and nerf-realized mapping. *arXiv preprint arXiv:2209.13274* (2022) [3](#)
11. Curless, B., Levoy, M.: Volumetric method for building complex models from range images. In: *SIGGRAPH Conference on Computer Graphics*. ACM (1996) [3](#), [9](#)
12. Dai, A., Chang, A.X., Savva, M., Halber, M., Funkhouser, T., Nießner, M.: ScanNet: Richly-annotated 3D reconstructions of indoor scenes. In: *Conference on Computer Vision and Pattern Recognition (CVPR)*. IEEE/CVF (2017). <https://doi.org/10.1109/CVPR.2017.261> [9](#), [11](#), [12](#), [13](#), [15](#), [18](#)
13. Dai, A., Nießner, M., Zollhöfer, M., Izadi, S., Theobalt, C.: Bundl fusion: Real-time globally consistent 3d reconstruction using on-the-fly surface reintegration. *ACM Transactions on Graphics (ToG)* **36**(4), 1 (2017) [1](#), [3](#), [6](#), [9](#)
14. Davison, A.J., Reid, I.D., Molton, N.D., Stasse, O.: Monoslam: Real-time single camera slam. *IEEE transactions on pattern analysis and machine intelligence* **29**(6), 1052–1067 (2007) [1](#)
15. Fuentes-Pacheco, J., Ruiz-Ascencio, J., Rendón-Mancha, J.M.: Visual simultaneous localization and mapping: a survey. *Artificial intelligence review* **43**, 55–81 (2015) [1](#)
16. Gao, Y., Cao, Y.P., Shan, Y.: Surfelnerf: Neural surfel radiance fields for online photorealistic reconstruction of indoor scenes. In: *Proceedings of the IEEE/CVF Conference on Computer Vision and Pattern Recognition*. pp. 108–118 (2023) [4](#)
17. Huang, H., Li, L., Cheng, H., Yeung, S.K.: Photo-slam: Real-time simultaneous localization and photorealistic mapping for monocular, stereo, and rgb-d cameras (2023) [4](#)
18. Huang, J., Huang, S.S., Song, H., Hu, S.M.: Di-fusion: Online implicit 3d reconstruction with deep priors. In: *IEEE/CVF Conference on Computer Vision and Pattern Recognition*. pp. 8932–8941 (2021) [1](#), [3](#)
19. Johnson, J., Douze, M., Jégou, H.: Billion-scale similarity search with GPUs. *IEEE Transactions on Big Data* **7**(3), 535–547 (2019) [9](#)
20. Kähler, O., Prisacariu, V., Valentin, J., Murray, D.: Hierarchical voxel block hashing for efficient integration of depth images. *IEEE Robotics and Automation Letters* **1**(1), 192–197 (2015) [3](#)
21. Kähler, O., Prisacariu, V.A., Ren, C.Y., Sun, X., Torr, P.H.S., Murray, D.W.: Very high frame rate volumetric integration of depth images on mobile devices. *IEEE Trans. Vis. Comput. Graph.* **21**(11), 1241–1250 (2015). <https://doi.org/10.1109/TVCG.2015.2459891>, <https://doi.org/10.1109/TVCG.2015.2459891> [3](#)
22. Kazerouni, I.A., Fitzgerald, L., Dooly, G., Toal, D.: A survey of state-of-the-art on visual slam. *Expert Systems with Applications* **205**, 117734 (2022) [1](#)
23. Keetha, N., Karhade, J., Jatavallabhula, K.M., Yang, G., Scherer, S., Ramanan, D., Luiten, J.: Splatam: Splat, track & map 3d gaussians for dense rgb-d slam. *arXiv preprint* (2023) [4](#), [10](#), [11](#), [12](#), [13](#), [14](#), [16](#), [17](#), [18](#)

24. Keller, M., Lefloch, D., Lambers, M., Izadi, S., Weyrich, T., Kolb, A.: Real-time 3d reconstruction in dynamic scenes using point-based fusion. In: International Conference on 3D Vision (3DV). pp. 1–8. IEEE (2013) [3](#)
25. Kerbl, B., Kopanas, G., Leimkühler, T., Drettakis, G.: 3d gaussian splatting for real-time radiance field rendering. *ACM Transactions on Graphics* **42**(4) (July 2023), <https://repo-sam.inria.fr/fungraph/3d-gaussian-splatting/> [1](#), [4](#), [5](#), [7](#)
26. Klein, G., Murray, D.: Parallel tracking and mapping for small ar workspaces. In: 2007 6th IEEE and ACM international symposium on mixed and augmented reality. pp. 225–234. IEEE (2007) [1](#)
27. Li, H., Gu, X., Yuan, W., Yang, L., Dong, Z., Tan, P.: Dense rgb slam with neural implicit maps. arXiv preprint arXiv:2301.08930 (2023) [3](#), [4](#)
28. Li, K., Tang, Y., Prisacariu, V.A., Torr, P.H.: Biv-fusion: Dense 3d reconstruction using bi-level neural volume fusion. In: IEEE/CVF Conference on Computer Vision and Pattern Recognition. pp. 6166–6175 (2022) [3](#)
29. Lin, C.H., Ma, W.C., Torralba, A., Lucey, S.: BARF: Bundle-Adjusting Neural Radiance Fields. In: International Conference on Computer Vision (ICCV). IEEE/CVF (2021). <https://doi.org/10.1109/ICCV48922.2021.00569> [3](#)
30. Liu, D., Chen, C., Xu, C., Qiu, R.C., Chu, L.: Self-supervised point cloud registration with deep versatile descriptors for intelligent driving. *IEEE Transactions on Intelligent Transportation Systems* (2023) [3](#)
31. Liu, L., Gu, J., Lin, K.Z., Chua, T.S., Theobalt, C.: Neural sparse voxel fields. In: *Advances in Neural Information Processing Systems*. vol. 33, pp. 15651–15663 (2020) [3](#)
32. Lorensen, W.E., Cline, H.E.: Marching cubes: A high resolution 3d surface construction algorithm. *ACM siggraph computer graphics* **21**(4), 163–169 (1987) [10](#)
33. Luiten, J., Kopanas, G., Leibe, B., Ramanan, D.: Dynamic 3d gaussians: Tracking by persistent dynamic view synthesis (2023) [4](#)
34. Mahdi Johari, M., Carta, C., Fleuret, F.: Eslam: Efficient dense slam system based on hybrid representation of signed distance fields. arXiv e-prints pp. arXiv–2211 (2022) [1](#), [2](#), [3](#), [4](#), [10](#), [11](#), [12](#), [13](#), [14](#), [17](#), [18](#)
35. Maier, R., Sturm, J., Cremers, D.: Submap-based bundle adjustment for 3d reconstruction from rgb-d data. In: *Pattern Recognition: 36th German Conference, GCPR 2014, Münster, Germany, September 2-5, 2014, Proceedings 36*. pp. 54–65. Springer (2014) [6](#)
36. Marniok, N., Johannsen, O., Goldluecke, B.: An efficient octree design for local variational range image fusion. In: *German Conference on Pattern Recognition (GCPR)*. pp. 401–412. Springer (2017) [3](#)
37. Matsuki, H., Murai, R., Kelly, P.H.J., Davison, A.J.: Gaussian splatting slam (2023) [4](#)
38. Mescheder, L., Oechsle, M., Niemeyer, M., Nowozin, S., Geiger, A.: Occupancy networks: Learning 3d reconstruction in function space. In: *IEEE/CVF conference on computer vision and pattern recognition*. pp. 4460–4470 (2019) [4](#)
39. Mihajlovic, M., Weder, S., Pollefeys, M., Oswald, M.R.: Deepsurfels: Learning on-line appearance fusion. In: *IEEE/CVF Conference on Computer Vision and Pattern Recognition*. pp. 14524–14535 (2021) [4](#)
40. Mildenhall, B., Srinivasan, P.P., Tancik, M., Barron, J.T., Ramamoorthi, R., Ng, R.: NeRF: Representing Scenes as Neural Radiance Fields for View Synthesis. In: *European Conference on Computer Vision (ECCV)*. CVF (2020). [https://doi.org/10.1007/978-3-030-58452-8\\_{\\_}24](https://doi.org/10.1007/978-3-030-58452-8_{_}24), [https://link.springer.com/10.1007/978-3-030-58452-8\\_24](https://link.springer.com/10.1007/978-3-030-58452-8_24)<http://arxiv.org/abs/2003.08934> [1](#), [3](#)

41. Müller, T., Evans, A., Schied, C., Keller, A.: Instant neural graphics primitives with a multiresolution hash encoding. *ACM Transactions on Graphics (ToG)* **41**(4), 1–15 (2022) [3](#)
42. Mur-Artal, R., Tardos, J.D.: ORB-SLAM2: An Open-Source SLAM System for Monocular, Stereo, and RGB-D Cameras. *IEEE Transactions on Robotics* **33**(5), 1255–1262 (2017). <https://doi.org/10.1109/TR0.2017.2705103> [1](#)
43. Murez, Z., van As, T., Bartolozzi, J., Sinha, A., Badrinarayanan, V., Rabinovich, A.: Atlas: End-to-end 3d scene reconstruction from posed images. In: *Computer Vision–ECCV 2020: 16th European Conference, Glasgow, UK, August 23–28, 2020, Proceedings, Part VII* 16. pp. 414–431. Springer (2020) [3](#)
44. Newcombe, R.A., Izadi, S., Hilliges, O., Molyneaux, D., Kim, D., Davison, A.J., Kohli, P., Shotton, J., Hodges, S., Fitzgibbon, A.W.: Kinectfusion: Real-time dense surface mapping and tracking. In: *ISMAR*. vol. 11, pp. 127–136 (2011) [1](#), [3](#)
45. Newcombe, R.A., Lovegrove, S.J., Davison, A.J.: Dtam: Dense tracking and mapping in real-time. In: *International Conference on Computer Vision (ICCV)* (2011) [1](#), [3](#)
46. Nießner, M., Zollhöfer, M., Izadi, S., Stamminger, M.: Real-time 3d reconstruction at scale using voxel hashing. *ACM Transactions on Graphics (TOG)* **32** (11 2013). <https://doi.org/10.1145/2508363.2508374> [1](#), [3](#)
47. Oechsle, M., Peng, S., Geiger, A.: UNISURF: Unifying Neural Implicit Surfaces and Radiance Fields for Multi-View Reconstruction. In: *International Conference on Computer Vision (ICCV)*. IEEE/CVF (2021). <https://doi.org/10.1109/ICCV48922.2021.00554>, <https://ieeexplore.ieee.org/document/9709919/> [3](#)
48. Oleynikova, H., Taylor, Z., Fehr, M., Siegwart, R., Nieto, J.I.: Voxblox: Incremental 3d euclidean signed distance fields for on-board MAV planning. In: *2017 IEEE/RSJ International Conference on Intelligent Robots and Systems, IROS 2017, Vancouver, BC, Canada, September 24-28, 2017*. pp. 1366–1373. IEEE (2017). <https://doi.org/10.1109/IROS.2017.8202315>, <https://doi.org/10.1109/IROS.2017.8202315> [3](#)
49. Ortiz, J., Clegg, A., Dong, J., Sucar, E., Novotny, D., Zollhoefer, M., Mukadam, M.: isdf: Real-time neural signed distance fields for robot perception. *arXiv preprint arXiv:2204.02296* (2022) [4](#)
50. Park, J., Zhou, Q.Y., Koltun, V.: Colored point cloud registration revisited. In: *Proceedings of the IEEE international conference on computer vision*. pp. 143–152 (2017) [15](#)
51. Peng, S., Niemeyer, M., Mescheder, L., Pollefeys, M., Geiger, A.: Convolutional Occupancy Networks. In: *European Conference Computer Vision (ECCV)*. CVF (2020), <https://www.microsoft.com/en-us/research/publication/convolutional-occupancy-networks/> [4](#)
52. Rosinol, A., Leonard, J.J., Carlone, L.: NeRF-SLAM: Real-Time Dense Monocular SLAM with Neural Radiance Fields. *arXiv* (2022), <http://arxiv.org/abs/2210.13641> [3](#)
53. Sandström, E., Li, Y., Van Gool, L., Oswald, M.R.: Point-slam: Dense neural point cloud-based slam. In: *International Conference on Computer Vision (ICCV)*. IEEE/CVF (2023) [1](#), [2](#), [4](#), [9](#), [10](#), [11](#), [12](#), [13](#), [14](#), [17](#), [18](#)
54. Sandström, E., Ta, K., Van Gool, L., Oswald, M.R.: Uncle-slam: Uncertainty learning for dense neural slam. In: *International Conference on Computer Vision Workshops (ICCVW)*. IEEE/CVF (2023) [3](#)
55. Sayed, M., Gibson, J., Watson, J., Prisacariu, V., Firman, M., Godard, C.: Simplercon: 3d reconstruction without 3d convolutions. In: *European Conference on Computer Vision*. pp. 1–19. Springer (2022) [3](#)

56. Schops, T., Sattler, T., Pollefeys, M.: BAD SLAM: Bundle adjusted direct RGB-D SLAM. In: CVF/IEEE Conference on Computer Vision and Pattern Recognition (CVPR) (2019) [1](#), [3](#), [4](#)
57. Steinbrucker, F., Kerl, C., Cremers, D.: Large-scale multi-resolution surface reconstruction from rgb-d sequences. In: IEEE International Conference on Computer Vision. pp. 3264–3271 (2013) [3](#)
58. Stier, N., Rich, A., Sen, P., Höllerer, T.: Vortex: Volumetric 3d reconstruction with transformers for voxelwise view selection and fusion. In: 2021 International Conference on 3D Vision (3DV). pp. 320–330. IEEE (2021) [3](#)
59. Straub, J., Whelan, T., Ma, L., Chen, Y., Wijnmans, E., Green, S., Engel, J.J., Mur-Artal, R., Ren, C., Verma, S., et al.: The replica dataset: A digital replica of indoor spaces. arXiv preprint arXiv:1906.05797 (2019) [9](#), [10](#), [11](#), [12](#), [13](#), [15](#), [16](#), [17](#)
60. Stückler, J., Behnke, S.: Multi-resolution surfel maps for efficient dense 3d modeling and tracking. Journal of Visual Communication and Image Representation **25**(1), 137–147 (2014) [6](#)
61. Stühmer, J., Gumhold, S., Cremers, D.: Real-time dense geometry from a handheld camera. In: Joint Pattern Recognition Symposium. pp. 11–20. Springer (2010) [1](#), [12](#), [15](#), [16](#), [18](#)
62. Sturm, J., Engelhard, N., Endres, F., Burgard, W., Cremers, D.: A benchmark for the evaluation of RGB-D SLAM systems. In: International Conference on Intelligent Robots and Systems (IROS). IEEE/RSJ (2012). <https://doi.org/10.1109/IROS.2012.6385773>, <http://ieeexplore.ieee.org/document/6385773/> [2](#), [9](#), [10](#), [11](#), [13](#)
63. Sucar, E., Liu, S., Ortiz, J., Davison, A.J.: iMAP: Implicit Mapping and Positioning in Real-Time. In: International Conference on Computer Vision (ICCV). IEEE/CVF (2021). <https://doi.org/10.1109/ICCV48922.2021.00617>, <https://ieeexplore.ieee.org/document/9710431/> [1](#), [3](#), [4](#), [9](#)
64. Sun, J., Xie, Y., Chen, L., Zhou, X., Bao, H.: Neuralrecon: Real-time coherent 3d reconstruction from monocular video. In: IEEE/CVF Conference on Computer Vision and Pattern Recognition. pp. 15598–15607 (2021) [3](#)
65. Tang, Y., Zhang, J., Yu, Z., Wang, H., Xu, K.: Mips-fusion: Multi-implicit-submaps for scalable and robust online neural rgb-d reconstruction. arXiv preprint arXiv:2308.08741 (2023) [1](#)
66. Wang, H., Wang, J., Agapito, L.: Co-slam: Joint coordinate and sparse parametric encodings for neural real-time slam. In: Proceedings of the IEEE/CVF Conference on Computer Vision and Pattern Recognition. pp. 13293–13302 (2023) [1](#), [4](#)
67. Wang, J., Wang, P., Long, X., Theobalt, C., Komura, T., Liu, L., Wang, W.: Neuris: Neural reconstruction of indoor scenes using normal priors. In: Computer Vision–ECCV 2022: 17th European Conference, Tel Aviv, Israel, October 23–27, 2022, Proceedings, Part XXXII. pp. 139–155. Springer (2022) [3](#), [4](#)
68. Wang, Z., Bovik, A.C., Sheikh, H.R., Simoncelli, E.P.: Image quality assessment: from error visibility to structural similarity. IEEE transactions on image processing **13**(4), 600–612 (2004) [8](#), [9](#)
69. Wang, Z., Wu, S., Xie, W., Chen, M., Prisacariu, V.A.: Nerf-: Neural radiance fields without known camera parameters. arXiv preprint arXiv:2102.07064 (2021) [3](#)
70. Weder, S., Schonberger, J., Pollefeys, M., Oswald, M.R.: Routedfusion: Learning real-time depth map fusion. In: IEEE/CVF Conference on Computer Vision and Pattern Recognition. pp. 4887–4897 (2020) [3](#)

71. Weder, S., Schonberger, J.L., Pollefeys, M., Oswald, M.R.: Neurfusion: Online depth fusion in latent space. In: IEEE/CVF Conference on Computer Vision and Pattern Recognition. pp. 3162–3172 (2021) [3](#)
72. Whelan, T., Leutenegger, S., Salas-Moreno, R., Glocker, B., Davison, A.: Elastic-fusion: Dense slam without a pose graph. In: Robotics: Science and Systems (RSS) (2015) [1](#), [3](#), [4](#)
73. Whelan, T., McDonald, J., Kaess, M., Fallon, M., Johannsson, H., Leonard, J.J.: Kintinuous: Spatially extended kinectfusion. In: Proceedings of RSS '12 Workshop on RGB-D: Advanced Reasoning with Depth Cameras (2012) [3](#)
74. Wu, G., Yi, T., Fang, J., Xie, L., Zhang, X., Wei, W., Liu, W., Tian, Q., Wang, X.: 4d gaussian splatting for real-time dynamic scene rendering (2023) [4](#)
75. Xu, Q., Xu, Z., Philip, J., Bi, S., Shu, Z., Sunkavalli, K., Neumann, U.: Point-nerf: Point-based neural radiance fields. In: IEEE/CVF Conference on Computer Vision and Pattern Recognition. pp. 5438–5448 (2022) [4](#)
76. Yan, C., Qu, D., Wang, D., Xu, D., Wang, Z., Zhao, B., Li, X.: Gs-slam: Dense visual slam with 3d gaussian splatting (2024) [4](#)
77. Yan, Z., Tian, Y., Shi, X., Guo, P., Wang, P., Zha, H.: Continual neural mapping: Learning an implicit scene representation from sequential observations. In: IEEE/CVF International Conference on Computer Vision (ICCV). pp. 15782–15792 (October 2021) [3](#), [4](#)
78. Yang, X., Li, H., Zhai, H., Ming, Y., Liu, Y., Zhang, G.: Vox-fusion: Dense tracking and mapping with voxel-based neural implicit representation. In: IEEE International Symposium on Mixed and Augmented Reality (ISMAR). pp. 499–507. IEEE (2022) [3](#), [10](#), [11](#), [12](#), [13](#), [14](#)
79. Yang, X., Ming, Y., Cui, Z., Calway, A.: Fd-slam: 3-d reconstruction using features and dense matching. In: 2022 International Conference on Robotics and Automation (ICRA). pp. 8040–8046. IEEE (2022) [4](#)
80. Yang, Z., Yang, H., Pan, Z., Zhu, X., Zhang, L.: Real-time photorealistic dynamic scene representation and rendering with 4d gaussian splatting (2023) [4](#)
81. Yang, Z., Gao, X., Zhou, W., Jiao, S., Zhang, Y., Jin, X.: Deformable 3d gaussians for high-fidelity monocular dynamic scene reconstruction (2023) [4](#)
82. Yeshwanth, C., Liu, Y.C., Nießner, M., Dai, A.: Scannet++: A high-fidelity dataset of 3d indoor scenes. In: Proceedings of the IEEE/CVF International Conference on Computer Vision. pp. 12–22 (2023) [9](#), [12](#), [13](#), [15](#), [16](#), [17](#), [18](#)
83. Zhang, H., Chen, G., Wang, Z., Wang, Z., Sun, L.: Dense 3d mapping for indoor environment based on feature-point slam method. In: 2020 the 4th International Conference on Innovation in Artificial Intelligence. pp. 42–46 (2020) [3](#)
84. Zhang, R., Isola, P., Efros, A.A., Shechtman, E., Wang, O.: The unreasonable effectiveness of deep features as a perceptual metric. In: IEEE conference on computer vision and pattern recognition. pp. 586–595 (2018) [9](#)
85. Zhang, Y., Tosi, F., Mottocchia, S., Poggi, M.: Go-slam: Global optimization for consistent 3d instant reconstruction. arXiv preprint arXiv:2309.02436 (2023) [1](#), [3](#), [4](#)
86. Zhou, Q.Y., Koltun, V.: Dense scene reconstruction with points of interest. ACM Transactions on Graphics (TOG) **32**(4), 120 (2013). <https://doi.org/10.1145/2461912.2461919> [3](#)
87. Zhou, Q.Y., Miller, S., Koltun, V.: Elastic fragments for dense scene reconstruction. Proceedings of the IEEE International Conference on Computer Vision pp. 2726–2733 (2013) [3](#)

88. Zhu, Z., Peng, S., Larsson, V., Cui, Z., Oswald, M.R., Geiger, A., Pollefeys, M.: Nicer-slam: Neural implicit scene encoding for rgb slam. arXiv preprint arXiv:2302.03594 (2023) [3](#)
89. Zhu, Z., Peng, S., Larsson, V., Xu, W., Bao, H., Cui, Z., Oswald, M.R., Pollefeys, M.: Nice-slam: Neural implicit scalable encoding for slam. In: IEEE/CVF Conference on Computer Vision and Pattern Recognition. pp. 12786–12796 (2022) [1](#), [3](#), [10](#), [11](#), [12](#), [13](#), [14](#), [18](#)
90. Zollhöfer, M., Stotko, P., Görnitz, A., Theobalt, C., Nießner, M., Klein, R., Kolb, A.: State of the art on 3d reconstruction with rgb-d cameras. In: Computer graphics forum. vol. 37, pp. 625–652. Wiley Online Library (2018) [3](#)
91. Zwicker, M., Pfister, H., Van Baar, J., Gross, M.: Surface splatting. In: Proceedings of the 28th annual conference on Computer graphics and interactive techniques. pp. 371–378 (2001) [6](#)